Nanoscale

PAPER

Published on 16 June 2026
Licence and permissions

Check for updates

Cite this: *Nanoscale*, 2026, **18**, 15674

Curved interfaces-enhanced oxygen reduction reaction by PtCo alloys anchored MOF-derived carbon

Yutong Shi,†[a] Zheyan Tang,†[a] Hongwei Zhao, *[a] Pengyi Sun,[a] Lixiang Li, *[a] Haifei Liu,[a] Jingang Zheng,[a] Lin Tao, [a] Han Zhang, [a] Fang Di,[a] Chengguo Sun, [a,b] Zhihao Yao,[c] Yanzhou Qin [d] and Baigang An *[a]

Received 15th April 2026,
Accepted 15th June 2026

DOI: 10.1039/d6nr01476c

rsc.li/nanoscale

Carbon supports employed in the oxygen reduction reaction (ORR) catalysts frequently exhibit crumpled, curled, or other curved morphological features. The local microenvironment generated by such curved interfaces and its impact on the electronic structure of active sites, as well as reaction kinetics, remain to be studied. Herein, the finite element method was employed to elucidate the evolution of the local catalytic microenvironment during the pyrolysis of ZIF-67 from the perspective of geometric distortion. The results revealed that moderate interfacial curvature can significantly enhance the local electric field strength and promote O_2 enrichment. Guided by the simulation results, MOF-derived carbon with an optimal curved configuration was constructed by controlling the pyrolysis temperature. After etching, metal-ion adsorption, and H_2 reduction, MOF-derived carbon materials loaded with PtCo alloy (PtCo/NCs) were obtained. As expected, the PtCo/NCs-900 sample with a moderately curved interface exhibited outstanding ORR performance, with a half-wave potential of 0.831 V and an activity retention of 91.7% after 50 000 s. Density functional theory calculations demonstrated that the curved interface in PtCo/NCs-900 induces electron redistribution, shifts the d-band center of Pt and optimizes the *OH desorption behavior, thereby lowering the O_2 diffusion barrier, facilitating electron transfer, and ensuring sufficient O_2 supply. As an air–cathode catalyst, the PtCo/NCs-900 sample delivered a peak power density of 159 mW cm^{-2} and a specific capacity of 837 mAh g^{-1}_{Zn}, demonstrating its potential for practical energy applications.

1. Introduction

Sustainable energy conversion technologies, such as fuel cells and metal–air batteries, provide important pathways for addressing global energy and environmental challenges.[1–5] Among them, the electrochemical oxygen reduction reaction (ORR) is a key process that governs device performance. However, its inherently sluggish reaction kinetics necessitates the use of highly efficient and durable catalysts.[6–8] Platinum (Pt) group metals possess excellent ORR activity, but their large-scale application is still hindered by high cost, limited natural abundance, and insufficient long-term stability.[9–11] Therefore, developing ORR catalysts with high performance and economic viability is critically important. One of the commonly adopted strategies is to reduce the size of Pt nanoparticles to maximize atomic utilization efficiency. However, size reduction is often accompanied by particle aggregation and ultimately compromises structural stability and catalytic performance.[12–16]

Noble-metal alloy catalysts such as platinum–cobalt (PtCo) alloy have attracted considerable attention due to their excellent catalytic performance.[17–21] The Co atoms in PtCo alloys can effectively adjust the electronic structure and surface composition of Pt, thereby significantly enhancing its intrinsic activity and atomic utilization while reducing the overall noble-metal loading amount.[22–24] Zeolitic imidazolate framework-67 (ZIF-67), formed by the coordination of Co^{2+} ions with imidazolate ligands, can serve as an ideal transition-metal precursor for constructing high-performance PtCo alloy catalysts owing to its well-defined porous framework and uniform coordination environment. An ordered pore architecture enables the *in situ* homogeneous dispersion of Co species within the framework and facilitates intimate contact and

[a]*Key Laboratory of Energy Materials and Electrochemistry Research Liaoning Province, School of Chemical Engineering, University of Science and Technology Liaoning, 189 Qianshanzhong Road, Anshan 114051, China.*
E-mail: hongwei0068@ustl.edu.cn, lxli2005@126.com, bgan@ustl.edu.cn
[b]*School of Chemical Engineering, Nanjing University of Science and Technology, Nanjing 210094, China*
[c]*High Temperature Materials Research Labs, School of Material Science and Engineering, University of Science and Technology Beijing, Beijing 100083, PR China*
[d]*State Key Laboratory of Engines, Tianjin University, Tianjin 300350, China*
†These authors contributed equally to this work and should be considered co-first authors.

diffusion between Pt and Co species during subsequent pyrolysis, thereby allowing for controlled alloying behavior.[25] Typically, approaches that involve infiltrating Pt precursors into ZIF-67 before pyrolysis to produce PtCo/N-doped carbon composites suffer from limited control over nanoparticle anchoring and interfacial architecture, weakening metal–support interactions and causing particle migration/agglomeration, structural degradation, and reduced catalytic efficiency.[26–29] Additionally, the ZIF-67-derived N-doped carbon support is pivotal. Its porous framework offers a high surface area and abundant anchoring sites while improving conductivity and chemical stability, thereby enhancing activity and durability.[30] However, PtCo sites generated by *in situ* pyrolysis are often embedded in or encapsulated by the carbon framework, which causes mass-transport and interfacial constraints. Consequently, the diffusion of O_2 and H^+/OH^- to the active sites is prolonged, and the effective three-phase contact is reduced, ultimately impeding the ORR kinetics.[31–33]

To address these issues, a structurally robust N-doped carbon framework needs to be constructed, followed by directional anchoring and precise regulation of the metal active sites on this framework. For example, Zhang *et al.* selectively etched the pyrolysis products of ZIF-67 to generate nitrogen-containing porous structures while removing large cobalt nanoparticles.[34] By exploiting micropore confinement effects and Pt–N coordination, they were able to precisely immobilize Pt atoms, which subsequently formed surface-anchored PtCo alloys on the carbon supports after thermal treatment in a reductive atmosphere. Huang *et al.* utilized the intrinsic hierarchical porosity of a ZIF-67-derived Co-NC framework to realize the uniform growth of PtCo nanoparticles.[35] By defect engineering, they tuned the electronic structure of the carbon supports and strengthened the interaction between the active sites and the support, thereby improving both the catalytic activity and stability. Notably, the N-doped carbon framework obtained from ZIF-67 pyrolysis often undergoes surface curvature reconstruction due to volumetric shrinkage, leading to geometric distortion and the formation of curved interfacial structures.[36] However, it remains unclear whether such curved interfaces can reshape the interfacial microenvironment, for example, by modulating the local electric field and driving the enrichment and transport of reactants at the curved interface to optimize the ORR kinetics.[37–39] Meanwhile, whether curved interfaces can further modify the electronic structure of PtCo alloy sites and regulate the adsorption/desorption behavior of reaction intermediates to enhance the ORR catalytic activity remains poorly understood.

Herein, we first employed the finite element method to construct models of the potential geometric distortions that may arise during ZIF-67 pyrolysis, which revealed that the formation of a moderately curved interface effectively enhances the local electric field and promotes O_2 enrichment. Guided by these simulations, nitrogen-doped carbon (NC) frameworks featuring curved interfaces were successfully fabricated *via* the temperature-controlled pyrolysis of ZIF-67. Catalysts with PtCo alloy nanoparticles anchored to N-doped carbon (PtCo/NCs) with different curved interfaces were synthesized. The PtCo/NCs-900 catalyst with a moderately curved interface exhibited excellent ORR activity ($E_{1/2}$ = 0.831 V) and durability. Density functional theory calculations reveal that curvature-driven electron redistribution upshifts the d-band center of Pt to optimize the desorption of *OH while mitigating the activation barrier of the rate-determining step. A moderately curved interface also guarantees highly efficient electron transfer and an abundant supply of O_2, thereby achieving a synergistic enhancement of the overall ORR kinetics. When applied in a Zn–air battery, the catalyst delivers an outstanding peak power density of 159 mW cm^{-2}, a specific capacity of 837 mAh g^{-1}_{Zn}, and robust rate performance.

2. Experimental section

2.1 Materials

Cobalt nitrate hexahydrate ($Co(NO_3)_2{\cdot}6H_2O$, 99%), sodium chloroplatinate ($Na_2[PtCl_6]{\cdot}6H_2O$), 2-methylimidazole (2-MI, 99%), polyvinyl pyrrolidone (PVP), potassium hydroxide (KOH, 90%), H_2SO_4 (98 wt%), ethanol (C_2H_5OH, 99.7%), and methanol (CH_3OH, 99.7%) were purchased from Aladdin Chemical Co., Ltd. All the reagents were used directly without further purification. O_2, N_2, and Ar were purchased from Liaoning Guoyi New Material Technology Co., Ltd. Commercial Pt/C (20 wt%) was purchased from Johnson-Matthey. The commercial 75% RuO_2 catalyst was obtained from Suzhou Sinero Technology Co., Ltd. Nafion solution (5 wt%) was purchased from DuPont. Deionized (DI) water was used in all experiments.

2.2 Synthesis of ZIF-67

0.67 g of 2-MI and 0.50 g of PVP were dissolved in 50 mL of methanol, followed by ultrasonication at room temperature to achieve a homogeneous solution A. Separately, 0.59 g of $Co(NO_3)_2{\cdot}6H_2O$ was dissolved in 50 mL of methanol to obtain solution B. Solutions A and B were then combined by adding the 2-MI/PVP mixture, which was added into the $Co(NO_3)_2$ solution under vigorous stirring for 1 min. The resulting reaction mixture was aged at room temperature for 12 h. The product was subsequently collected *via* centrifugation, followed by vacuum filtration, and dried overnight at 50 °C to yield dodecahedral ZIF-67.

2.3 Synthesis of Co NPs/NCs and Co/NCs

ZIF-67 particles were dispersed in a ceramic boat and heated to 350 °C in a tube furnace for 1.5 h, then increased to different temperatures (700, 800, 900, and 1000 °C) at a heating rate of 5 °C min^{-1} and maintained for 3.5 h. The pyrolysis process was carried out in a N_2 atmosphere. Co-loaded N-doped carbons with large Co nanoparticles (Co NPs/NCs-*X*, *X* = 700, 800, 900, and 1000) were synthesized at different pyrolysis temperatures. Subsequently, Co NPs/NCs-*X* was subjected to treatment in 0.5 M H_2SO_4 solution for 3 h, followed by centrifugation and drying to selectively remove the large Co

nanoparticles and obtain Co-loaded N-doped carbons containing only small Co nanoparticles (Co/NCs-*X*).

2.4 Synthesis of PtCo/NCs

100 mg Co/NCs-*X* and 1 mL $Na_2[PtCl_6]$ (2.16 g mL^{-1}) were added into 10 mL DI water, stirred at 60 °C for 6 h, then centrifuged and vacuum dried at 60 °C to obtain Co@Pt/NCs-*X*. The Co@Pt/NCs-*X* was heat treated at 700 °C for 2 h in a H_2 (5 vol%)/Ar (95 vol%) atmosphere in a horizontal tubular furnace to form a PtCo alloy. The final sample was named PtCo/NCs-*X* (*X* = 700, 800, 900, and 1000).

2.5 Finite element simulation

The finite element method (FEM) was employed to systematically analyze the evolution of the physical fields in ZIF-67 during thermally induced deformation. Based on the potential deformation states under heat treatment, four kinds of 2D hexagonal models with a side length of 500 nm (denoted as Def-1, Def-2, Def-3, and Def-4) were constructed. Their geometric surfaces were adjusted to simulate varying degrees of curved interface. Regarding the electric field simulations, a uniform external field was applied across the computational domain to investigate the localized field enhancement induced by the deformed interfaces. Furthermore, an oxygen transport model based on Fick's laws of diffusion was established to quantitatively analyze the electric field distribution and oxygen aggregation behavior on the surfaces of models with different deformation levels.

2.6 Sample characterization

The morphology and structure of the catalyst were characterized by scanning electron microscopy (SEM, FEI Apreo, 1 kV), scanning transmission electron microscopy (STEM, FEI Apreo, 10 kV) and high-resolution transmission electron microscopy (HRTEM, JEOL, JEM-F200). The crystallization information of the material in the range of 2θ of 5–90° was collected using an X-ray diffractometer (XRD, Rigaku D/MAX-2500X). Raman spectra were obtained using a confocal Raman device (HORIBA, Xplora Plus), and defects in the carbon material and the degree of graphitization were observed. The nitrogen adsorption/desorption isotherms of the samples at −196 °C were determined using the ASAP-2020 adsorption/desorption device, and the pore volumes were calculated using the non-local density functional theory (NLDFT). The chemical states were analyzed using X-ray photoelectron spectroscopy (XPS, Shimadzu, AXIS SUPRA, Al Kα). The quantitative analysis of the target metallic elements (Pt and Co) in the catalysts was performed using an inductively coupled plasma optical emission spectrometer (ICP-OES).

2.7 Electrochemical measurements

Electrochemical tests were performed using a three-electrode setup of a DH7003 electrochemical workstation (DONGHUA). The electrodes used were a glass carbon electrode (working electrode), Ag/AgCl chloride electrode (reference electrode), and Pt sheet (counter electrode).

To prepare a uniform catalyst ink, 5.0 mg of the catalyst powder was ultrasonically dispersed in a solvent mixture containing 500 μL of ethanol, 450 μL of deionized water, and 50 μL of Nafion solution (5 wt%) in an ice bath for 30 min. Subsequently, the well-dispersed ink was drop-cast onto a rotating disk electrode (RDE, 0.1256 cm^2) with 10 μL and a rotating ring-disk electrode (RRDE, disk: 0.2475 cm^2, ring: 0.1866 cm^2) with 20 μL, yielding a catalyst loading of approximately 0.40 mg cm^{-2} in both cases.

All potentials reported in this work are referenced to reversible hydrogen electrodes (RHEs): $E_{RHE} = E_{Ag/AgCl} + 0.0591\ pH + 0.198$. The ORR performance of the catalyst was investigated using cyclic voltammetry (CV) and linear scanning voltammetry (LSV). CVs were recorded at a scan rate of 50 mV s^{-1}. The LSV was measured at a scan rate of 10 mV s^{-1} at 400, 625, 900, 1225, 1600, 2025, and 2500 rpm. The electrolyte was purged with pure N_2 or O_2 gas (at least 30 min) before electrochemical testing. The electron transfer number (n) and hydrogen peroxide yield (H_2O_2%) were computed based on the RRDE test results:

$$n = \frac{4I_D}{I_D + I_R/N},$$

$$H_2O_2\% = \frac{I_R/N}{I_D + I_R/N} \times 200\%,$$

where I_D is the disk current, I_R is the ring current, and N (N = 0.37) is the current collection efficiency of the Pt ring.

For the kinetic analysis of the catalyst, the Koutecky–Levich equation was used in this work:

$$\frac{1}{j} = \frac{1}{j_k} + \frac{1}{j_l} = \frac{1}{j_k} + \frac{1}{B\omega^{1/2}},$$

$$B = 0.2nFC_0D_0^{2/3}\nu^{-1/6},$$

$$j_k = nFkC_0,$$

where j represents the obtained current density, j_k represents the kinetic current density, j_l represents the current density that was limiting diffusion, n represents the reaction's total number of O_2 electron transfers, F is the Faraday constant (96 485 C mol^{-1}), and ω is the angular velocity of the rotation rate of the disc. The volumetric concentration of oxygen was C_0 (1.9×10^{-5} cm^2 s^{-1}), the diffusion coefficient of O_2 was D_0 (1.2×10^{-6} mol cm^{-3}), and ν was the kinematic viscosity of the electrolyte (0.01 cm^2 s^{-1}).

The mass activity (j_m, mA mg^{-1}) of the prepared catalysts was calculated according to the following equation: $j_m = j_k/(w_{metal} \times c_{catal})$, where j_k is the kinetic current density, w_{metal} is the weight fraction of the metal species determined by ICP-OES, and c_{catal} represents the catalyst loading on the electrode. The turnover frequency (TOF, e per s per site) was evaluated using the following equation:

$$TOF = j_kN_eM_{metal}/(N_aw_{metal}c_{catal})$$

where N_e is the number of electrons per Coulomb (6.24×10^{18} e C^{-1}), M_{metal} is the average molar mass of the metal, and N_a is the Avogadro constant (6.022×10^{23} mol^{-1}).

Primary Zn–air batteries (ZABs) were tested in a two-electrode system using 6.0 M KOH and 0.2 M $(CH_3COO)_2Zn$ aqueous electrolytes. Catalyst ink (without carbon black) was applied onto carbon fiber paper to create an air electrode with a load capacity of approximately 0.3 mg cm^{-2}. The anode was a polished Zn plate with a thickness of 0.2 mm.

3. Results and discussion

Given the geometric deformation and curved interface formation induced by volume shrinkage during ZIF-67 pyrolysis, four kinds of 2D physical models were first constructed using the finite element method (FEM) simulation to simulate the potential deformation characteristics. Fig. S1 depicts the geometric models of Def-1 to Def-4. It is observed that the edge curvature increases progressively from Def-1 to Def-4, eventually leading to structural collapse. These models can accurately reflect the deformation evolution of ZIF-67 with increasing pyrolysis temperatures, where the intensification of structural distortion ultimately results in framework failure. Fig. 1a shows the electric field distribution on the surface of the models. The results indicate that Def-1 and Def-2, lacking distinct curved interfaces, exhibit pronounced electric-field enhancement at the particle tips. As the degree of curvature increases, the enhanced electric field region gradually shifts from the tip to the curved interface. For Def-3, the tip-enhanced electric field remains, while the electric-field intensity on the curved surface is markedly increased. Notably, Def-4 with structural deterioration shows a non-uniform electric field distribution. Fig. 1b illustrates that the intensity drop (ΔE) from the vertex to the edge decreases significantly as the degree of deformation increases. Notably, Def-3 reaches the minimum ΔE, suggesting that the curved interface effectively enhances the localized electric field strength. However, the ΔE of Def-4 is markedly higher than that of the other models, indicating that the continuity and uniformity of the interfacial electric field distribution are disrupted by structural failure. Fig. 1c shows the rate of change in electric field intensity within the black-circled region indicated in Fig. 1a. The results show that the variation rate for Def-3 is only 1.3%, which is markedly lower than the other models. This further confirms that the formation of a moderately curved interface can effectively optimize the electric field distribution on the particle surface, thereby achieving an electric field-enhancement effect.

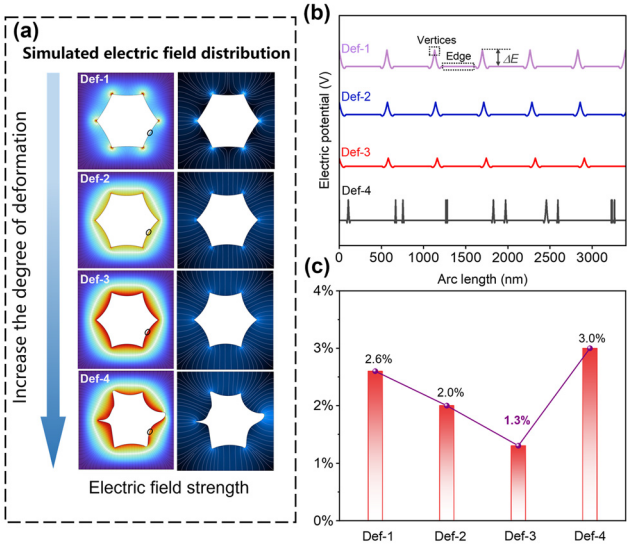

Fig. 1 FEM simulation. (a) Simulated electric field distribution, (b) curves depicting the change in electric field intensity from the vertex to the edge, and (c) rate of change of the electric field intensity within the specified region (indicated in black in a) for models with varying degrees of deformation: Def-1, Def-2, Def-3, and Def-4.

To further investigate the impact of interfacial deformation on O_2 mass transfer kinetics, the temporal distribution of O_2 concentration on the surfaces of various models was simulated using FEM (Fig. 2a). The results indicate that at all monitored time points, the curved interface of Def-3 exhibits a significantly higher degree of O_2 concentration enrichment compared to the other models. Fig. 2b depicts the surface O_2 concentration over time on the different curves, further confirming that Def-3 maintains a consistently higher concentration than the other models. Fig. 2c compares the time required for each model to reach specific O_2 concentrations (0.5 and 1.0 mmol nm^{-3}). Def-3 required the shortest duration to achieve the target levels, demonstrating the superiority of its moderately curved interface in accelerating the O_2 accumulation. Driven by the synergistic effect of localized electric field enhancement and O_2 enrichment at curved interfaces, the construction of a moderately curved interface in ZIF-67-derived carbon supports can significantly optimize the local catalytic microenvironment. It is foreseeable that this improved microenvironment can facilitate electron transfer between the substrate and active sites while ensuring an abundant supply of reactants to the catalytic sites.

Guided by the structures predicted *via* FEM simulations, the curved surface of ZIF-67 was effectively modulated through control of the pyrolysis temperature (700, 800, 900, and 1000 °C), enabling the high-quality replication of the simulated deformation configurations. Meanwhile, using pyrolyzed ZIF-67-derived carbon as N-doped carbon supports, PtCo alloy catalysts anchored onto N-doped carbon supports with distinct curved interfaces (PtCo/NCs-*X*) were successfully synthesized through a sequence of etching, ion adsorption, and H_2 reduction, where *X* denotes the specific pyrolysis temperature (Fig. 3). The as-prepared PtCo/NCs-*X* exhibit structural characteristics highly consistent with the models predicted. Correspondingly, a locally enhanced electric field and facilitated O_2 enrichment induced by the catalyst could be expected to accelerate the kinetics of the ORR and improve overall catalytic performance.

ZIF-67 appeared to have a smooth surface and a well-defined dodecahedral structure (Fig. 4a and Fig. S2). For Co NPs/NCs-900 prepared at 900 °C, the overall morphology was largely preserved after high-temperature pyrolysis, but a small

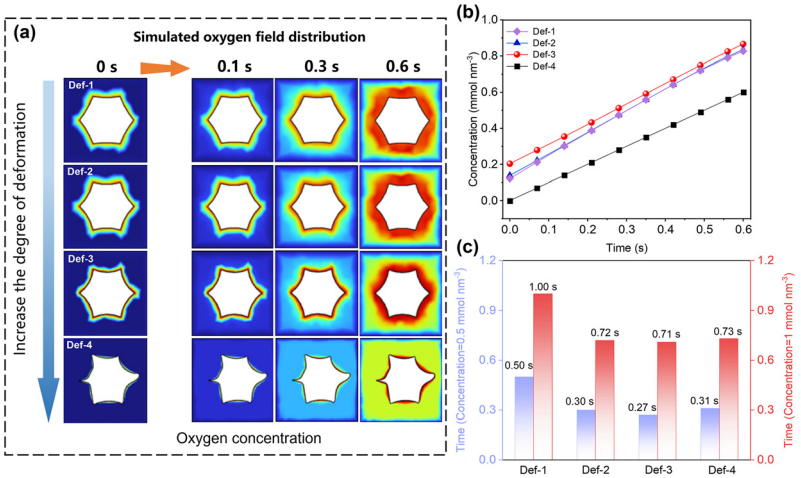

Fig. 2 Finite element simulation. (a) 2D models of O_2 distribution changes over time, (b) temporal variation in oxygen concentration within the model; and (c) time required to reach a specific O_2 concentration for models with varying degrees of deformation: Def-1, Def-2, Def-3, and Def-4.

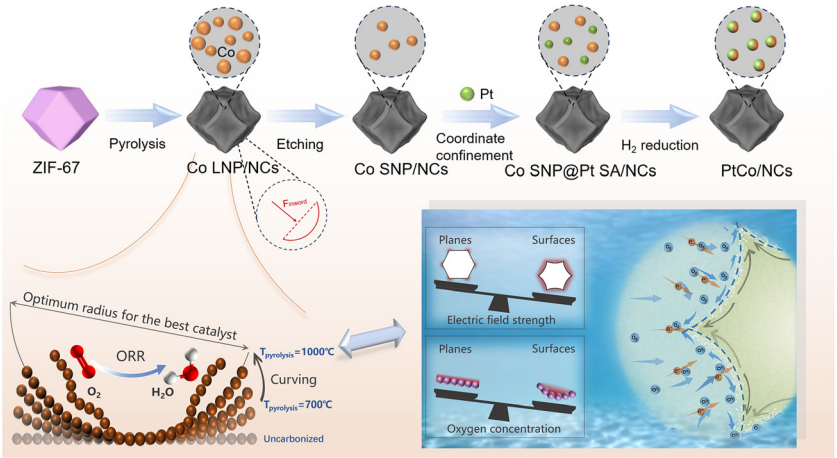

Fig. 3 Schematic of the synthesis of PtCo/NCs-*X* and its synergistic mechanism of local electric field and O_2 enrichment.

amount of whisker-like carbon nanotubes growing by Co catalysis can be observed on the surface of the sample (Fig. S3). Scanning transmission electron microscopy (STEM) images further revealed some large metal nanoparticles within Co NPs/NCs-900 (Fig. S4). Following acid washing, the external morphology of Co/NCs-900 remained unchanged. In contrast, the large internal metal nanoparticles were selectively removed, yielding a porous architecture with uniformly distributed cobalt nanoparticles or clusters (Fig. S5). This process also generated carbon defects and N-containing voids. PtCo/NCs-900 synthesized from Co/NCs-900 retained the overall morphological characteristics of Co NPs/NCs-900. However, mechanical stirring during the acid washing process led to the removal of loosely attached carbon nanotubes, thereby substantially reducing their surface density and revealing a distinctly curved surface morphology (Fig. 4b).

To verify the consistency between the curved interfaces of PtCo/NCs-*X* with different pyrolysis temperatures and the theoretical models, STEM was used to characterize the morphologies of the samples. As shown in Fig. 4c and Fig. S6, PtCo/NCs-700 and PtCo/NCs-800 exhibit nearly flat surfaces without discernible inward curvature. Upon increasing the pyrolysis temperature to 900 °C, a distinct concave curved interface appeared on the surface of PtCo/NCs-900. In contrast, further increasing the temperature to 1000 °C resulted in severe surface contraction in PtCo/NCs-1000, ultimately causing the structure to collapse. The corresponding schematic illustration (Fig. 4d) provides an intuitive visualization of the morphological evolution of the samples as a function of pyrolysis temperature. Evidently, the moderate concavity displayed by PtCo/NCs-900 is highly consistent with the optimized Def-3 model from FEM simulations. This geometric distortion can not only reshape the surface charge distribution at a physical level, thereby generating a significant localized field enhancement effect, but also create favorable space for O_2 capture and accumulation. Compared to low-curvature

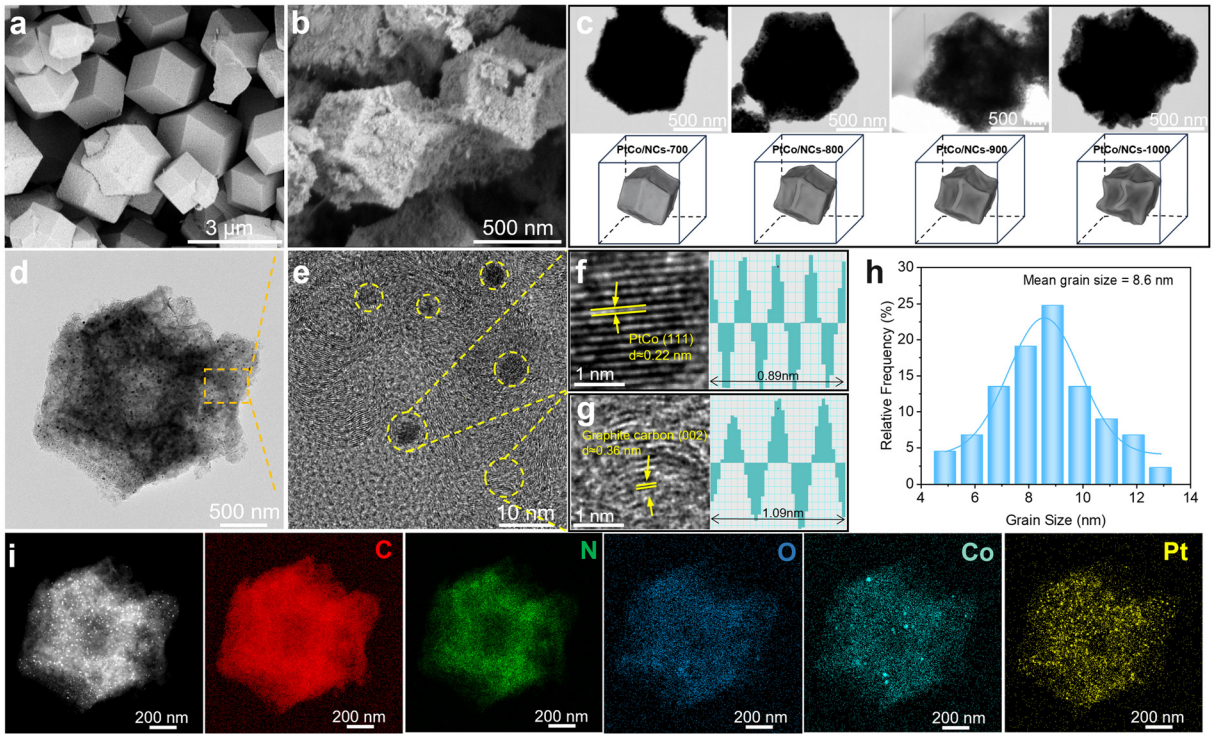

Fig. 4 Morphological characterization. (a and b) SEM images of ZIF-67 and PtCo/NCs-900. (c) STEM images and 3D models of different PtCo/NC-*X* samples. (d) TEM images, (e, f and g) HRTEM images, (h) nanoparticle size distribution, and (i) EDS mappings of PtCo/NCs-*X*.

samples (PtCo/NCs-700 and PtCo/NCs-800) and the collapsed structure caused by over-contraction (PtCo/NCs-1000), this intermediate curved interface is expected to optimize the local catalytic microenvironment and synergize with PtCo active sites, enhancing the overall performance of the catalyst.

HRTEM was employed to gain insight into the internal microstructure of PtCo/NCs-900. As shown in Fig. 4e, a large number of metal nanoparticles are uniformly distributed throughout the interior of PtCo/NCs-900. Upon further magnification (Fig. 4f), these nanoparticles display well-defined crystalline features with clearly resolved lattice fringes. The measured interplanar spacing of approximately 0.22 nm can be assigned to the (111) plane of the tetragonal PtCo alloy (Fig. 4g).[40] Moreover, the PtCo alloy nanoparticles are encapsulated by amorphous, onion-like carbon layers, which exhibit lattice fringes with an interlayer spacing of about 0.36 nm, corresponding to the (002) plane of graphitic carbon (Fig. 4h).[41] This type of graphitized carbon layer has relatively high electronic conductivity, thereby facilitating efficient charge transfer during the electrocatalytic process. Statistical analysis of the nanoparticle size distribution indicates that the metal nanoparticles are predominantly centered at approximately 9.0 nm (Fig. 4i). In addition, elemental mapping reveals that C, O, N, Pt, and Co are uniformly distributed throughout PtCo/NCs-900 (Fig. 4j), with the spatial distributions of Pt and Co exhibiting nearly complete overlap, thereby confirming the successful formation of the PtCo alloy. This observation can be attributed to the effective alloying of Pt and Co within the confined space, indicating that the secondary pyrolysis reduction process plays a crucial role in facilitating the formation of the alloy phase.

The crystalline nature of the PtCo alloy was confirmed by powder X-ray diffraction (XRD). As shown in Fig. 5a, the diffraction patterns for all samples match well with the JCPDS card (no. 43-1358) for the PtCo alloy. The characteristic peaks at 41.6°, 49.3°, 69.7° and 84.7° can be indexed to the (111), (200), (220) and (311) planes of the PtCo alloy,[42] respectively, unambiguously confirming the formation of the alloy phase. Notably, although the Co nanoparticles within the acid-leached Co/NCs-*X* matrix remain confined by a carbonaceous shell, intrinsic defects and pores generated during pyrolysis facilitate the penetration and adsorption of the Pt precursor. During the subsequent high-temperature treatment, the H_2 atmosphere not only reduces the Pt precursors into highly mobile metallic Pt atoms but also mildly etches the defective carbon layers, creating additional nanoscale diffusion channels. Driven by the elevated temperature, Pt atoms migrate and react at the interface with the confined Co core, ultimately forming a well-defined PtCo alloy.[11,43] Meanwhile, a prominent diffraction peak assigned to the graphite (002) plane was observed for all samples, indicating that ZIF-67 was converted into graphitic carbon upon high-temperature pyrolysis.[44] The graphitization degree of the materials was evaluated using Raman spectroscopy (Fig. 5b). All samples exhibit two characteristic bands corresponding to defective sp^3 carbon and graphitic sp^2 carbon at approximately 1350 cm^{-1} (D band) and

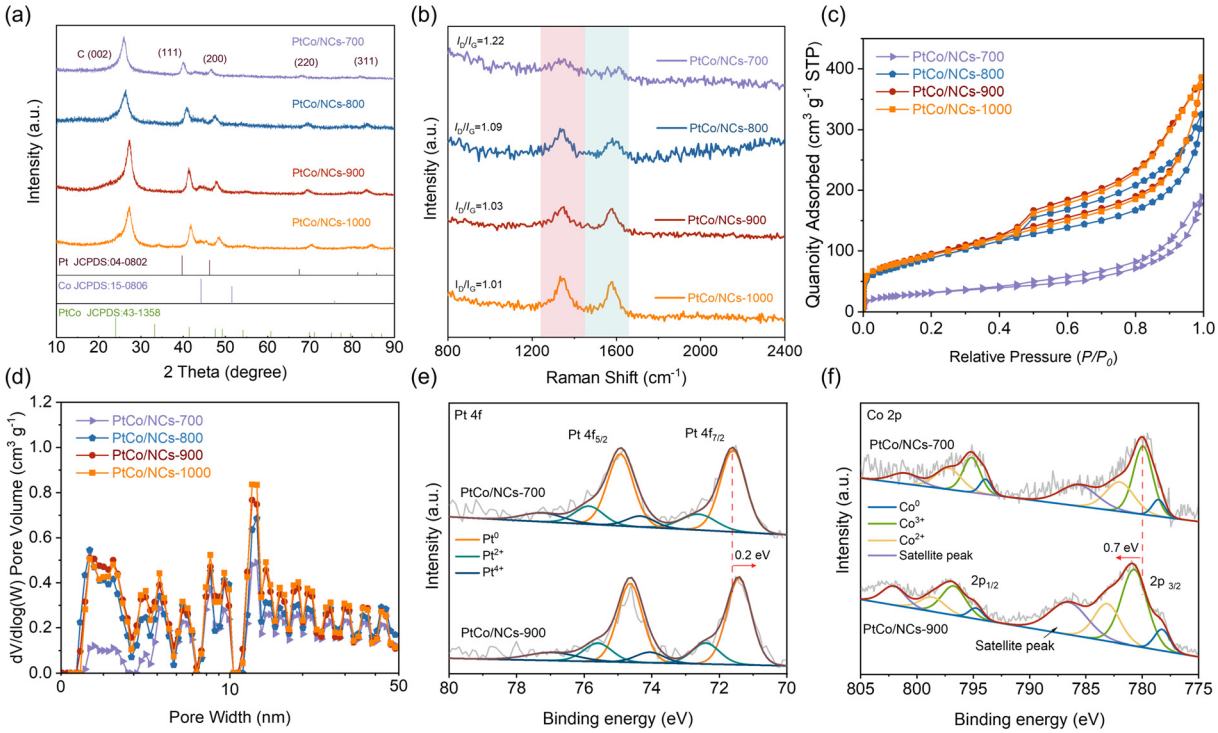

Fig. 5 (a) XRD patterns, (b) Raman spectra, (c) N_2 adsorption isotherms, and (d) pore size distribution of PtCo/NCs-*X*. (e and f) XPS spectra of Pt 4f and Co 2p of PtCo/NCs-900.

1590 cm^{-1} (G band), respectively.[45] The I_D/I_G value of the samples indicates that increasing the pyrolysis temperature enhances the structural order of carbon, which is beneficial for electron transfer during the reaction process.

N_2 adsorption–desorption isotherms of PtCo/NCs-*X* samples were measured at −196 °C. As illustrated in Fig. 5c, all samples displayed a hysteresis loop at a middle to high relative pressure (P/P_0 = 0.5) with type IV isotherm characteristics, indicating that the materials possess a mesoporous structure.[46] Fig. 5d depicts the pore size distribution curves of the PtCo/NCs-*X* samples. The content of micropores smaller than 2 nm is relatively low in PtCo/NCs-700, whereas it is higher and nearly identical in the other three samples. Notably, PtCo/NCs-900 and PtCo/NCs-1000 contain much more mesopores than PtCo/NCs-700 and PtCo/NCs-800. The evolution of these pores is attributed to the profound carbonization of ligands and the thermally driven behavior of Co nanoparticles. When the temperature is around 800 °C, the decomposition and volatilization of ligands act as pore-formers, generating an extensive micropore network. Upon increasing the temperature to 900–1000 °C, the intensified aggregation and ripening of Co nanoparticles leave behind larger spatial voids following subsequent acid etching. The severe shrinkage of the carbon framework coupled with the merging of adjacent micropores at higher temperatures leads to a significant surge in the proportion of mesopores within the 11–14 nm range. Meanwhile, as shown in Table S1, the S_{BET} of PtCo/NCs-700 is relatively low (113.8 m^2 g^{-1}). With increasing pyrolysis temperature, the S_{BET} of PtCo/NCs-800, PtCo/NCs-900, and PtCo/NCs-1000 increase markedly, reaching approximately 326.8, 346.8, and 336.0 m^2 g^{-1}, respectively. This result suggests that higher pyrolysis temperatures promote the development of a porous carbon framework. Further analysis reveals that as the pyrolysis temperature increases from 800 °C to 1000 °C, the S_{micro} gradually decreases, whereas the S_{meso} increases steadily. As a result, the S_{meso}/S_{BET} ratio rises from 52.6% to 63.9%. Consequently, PtCo/NCs-900 combines moderate curved interfaces with superior S_{BET} and favorable pore distribution, which could optimize the local catalytic microenvironment and thus contribute to both the mass transfer kinetic efficiency and active site utilization of the catalyst during the ORR process.

To investigate the effect of a curved interface on the chemical state of the carbon supports and PtCo alloy, XPS measurements were conducted on samples without obvious curvature (PtCo/NCs-700) and with a pronounced curved interface (PtCo/NCs-900). The XPS spectra confirmed the presence of C, N, O, Pt and Co elements in PtCo/NCs-700 and PtCo/NCs-900 (Fig. S7a). High-resolution N 1s spectra reveal that PtCo/NCs-700 and PtCo/NCs-900 contain high levels of pyridinic-N, pyrrolic-N, graphitic-N, and oxidized-N at 398.6 eV, 399.9 eV, 400.9 eV, and 402.0 eV (Fig. S7b), respectively.[47,48] Deconvolution of C 1s spectra indicates the existence of C–C/C=C, C–N and C=O bonds.[48] Notably, the binding energies of the C–N and C=O bonds in PtCo/NCs-900 exhibit a negative shift of approximately 0.3 eV compared to those of PtCo/NCs-700 (Fig. S7c), suggesting an electron transfer from the surround-

ing environment to the carbon–nitrogen interface. This phenomenon can be attributed to the fact that the curved interface alters the electronic structure of the carbon supports. The characteristic concave curvature of PtCo/NCs-900 breaks the symmetry of the charge distribution within the carbon layers, inducing the geometric distortion of the sp^2 orbitals. This charge redistribution, triggered by geometric deformation and synergized with the localized electric field intensification confirmed by FEM simulations, can create a more potent electron-trapping capability. Consequently, it promotes electron accumulation at the interface, ultimately leading to a negative shift in binding energy.

Chemical alterations in the supported PtCo alloy can be identified through high-resolution XPS spectra. As shown in Fig. 5e, the high-resolution XPS spectra of Pt 4f can be deconvoluted into three distinct chemical states, corresponding to Pt^0, Pt^{2+}, and Pt^{4+} species, where the presence of the high-valence species is attributed to surface oxidation.[47] Compared with PtCo/NCs-700, the PtCo/NCs-900 catalyst displays a positive shift of approximately 0.20 eV. However, the high-resolution Co XPS exhibits an approximately 0.7 eV negative energy shift in the PtCo/NCs-900 catalyst (Fig. 5f). All the above shifts indicate that in PtCo/NCs-900, due to the existence of the curved interface, there is a strong electronic interaction between Pt and Co, consistent with the subsequent projected density of states analysis. This strong electronic interaction causes a shift in the d-center of the Pt atom, which optimizes the binding strength of oxygen-containing intermediates and thereby accelerates the kinetics of the ORR. Meanwhile, electron accumulation at the curved interface strengthens the interaction between the PtCo alloy and the curved carbon supports to facilitate interfacial charge transfer, thus synergistically enhancing catalytic activity and structural durability.[49] Additionally, inductively coupled plasma atomic emission spectrometry (ICP-OES) indicates that the Pt and Co element contents of PtCo/NCs-900 are 3.95 and 1.80 wt%, respectively, which are close to those in other samples (Fig. S8). The lower Pt content significantly reduces noble-metal usage and overall material costs, thereby improving cost-effectiveness.

The ORR performance of the samples was evaluated by cyclic voltammetry (CV) using a standard three-electrode electrochemical system (Fig. 6a and Fig. S9). A distinct ORR peak was observed for all samples in O_2-saturated 0.1 M KOH electrolyte, indicating that all samples possess the ORR catalytic activity. This result is further corroborated by linear sweep voltammetry (LSV) curves obtained from rotating disk electrode (RDE) measurements (Fig. 6b). PtCo/NCs-900 achieves a limiting current density of 5.65 mA cm^{-2}, which is higher than that of Pt/C (5.1 mA cm^{-2}). It also exhibits a half-wave potential ($E_{1/2}$ = 0.831 V), which is almost the same as that of Pt/C ($E_{1/2}$ = 0.824 V) and is substantially higher than those of PtCo/NCs-700 ($E_{1/2}$ = 0.749 V), PtCo/NCs-800 ($E_{1/2}$ = 0.814 V), and PtCo/NCs-1000 ($E_{1/2}$ = 0.807 V). To isolate the specific contribution of the support architecture from the noble metal alloying effect, Pt-free control samples were investigated (Fig. S10). The ORR performance of Co/NCs-*X* samples exhibits a clear trend with pyrolysis temperature. Co/NCs-900 delivers optimal intrinsic catalytic activity among the control groups. This result demonstrates that the pyrolysis-temperature-dependent curvature of the carbon matrix plays a fundamental and dominant role in regulating the local reaction microenvironment. These observed performance differences are primarily dictated by the pyrolysis temperature-dependent structure and geometry of the carbon supports.

The lackluster activity of PtCo/NCs-700 and PtCo/NCs-800 is hampered by incomplete carbonization, immature hierarchical porosity and low surface curvature, resulting in restricted site accessibility and negligible localized microenvironment. In contrast, the extreme temperature of 1000 °C triggers excessive framework shrinkage and structural collapse likely burying or aggregating PtCo active sites and disrupting the optimized catalytic microenvironment. Notably, PtCo/NCs-900 achieves a synergistic optimum, where its hierarchical porosity and tailored curved interface collectively boost mass transfer kinetics and site accessibility. Furthermore, the ORR activity of PtCo/NCs-900 is markedly higher than that of its base material (Co/NCs-900, $E_{1/2}$ = 0.799 V). This indicates that, under identical curved interface structures, the formation of highly active PtCo alloy sites also plays a significant role in enhancing catalytic performance, working in synergy with the optimized local microenvironment to markedly elevate the ORR activity.

Moreover, the kinetic current density (j_k at 0.80 V) of PtCo/NCs-900 was calculated to be 15.2 mA cm^{-2}, which is 1.31 times larger than that of Pt/C and significantly higher than those of the other samples (Fig. 6c). Meanwhile, based on these LSV results (Fig. S11a–e), Koutecky–Levich (K–L) plots of all samples appear to have a linear correlation (Fig. S10f–j).[50] As shown in Fig. 6d, the faster kinetics of PtCo/NCs-900 are evidenced by its lowest Tafel slope (64 mV dec^{-1}) than PtCo/NCs-700 (86 mV dec^{-1}), PtCo/NCs-800 (67 mV dec^{-1}) and PtCo/NCs-1000 (72 mV dec^{-1}). The electrochemically active surface area (ECSA) of PtCo/NCs-*X* can be evaluated using double-layer capacitance (C_{dl}) to reflect the accessible active sites of the samples. As shown in Fig. S12, the calculated C_{dl} value for PtCo/NCs-900 is 7.02 mF cm^{-2} (Fig. 6e), which is significantly higher than those of PtCo/NCs-700 (1.16 mF cm^{-2}), PtCo/NCs-800 (6.18 mF cm^{-2}) and PtCo/NCs-1000 (4.03 mF cm^{-2}). Rotating ring-disk electrode (RRDE) measurements were conducted to elucidate the ORR selectivity of PtCo/NCs-*X* catalysts. As shown in Fig. 6f and Fig. S13, PtCo/NCs-900 exhibits the lowest H_2O_2 yield (9.1%) and an electron transfer number close to 3.80, which are superior to those of PtCo/NCs-700 (3.54% and 24.2%), PtCo/NCs-800 (3.74% and 13.5%), and PtCo/NCs-1000 (3.62 and 18.9%). The high selectivity of PtCo/NCs-900 toward the four-electron ORR pathway and its low H_2O_2 by-product yield not only ensures high energy conversion efficiency but also mitigates catalyst degradation caused by oxygen-containing radical species. Meanwhile, as shown in Table 1, PtCo/NCs-900 exhibited much higher mass activity (j_m, 907.87 mA mg^{-1}) and turnover frequency (TOF, 4.44 e^- per site per s) at 0.80 V than PtCo/NCs-700 (j_m = 57.14 mA mg^{-1}, TOF = 0.28 e^- per site per s), PtCo/NCs-800 (j_m =

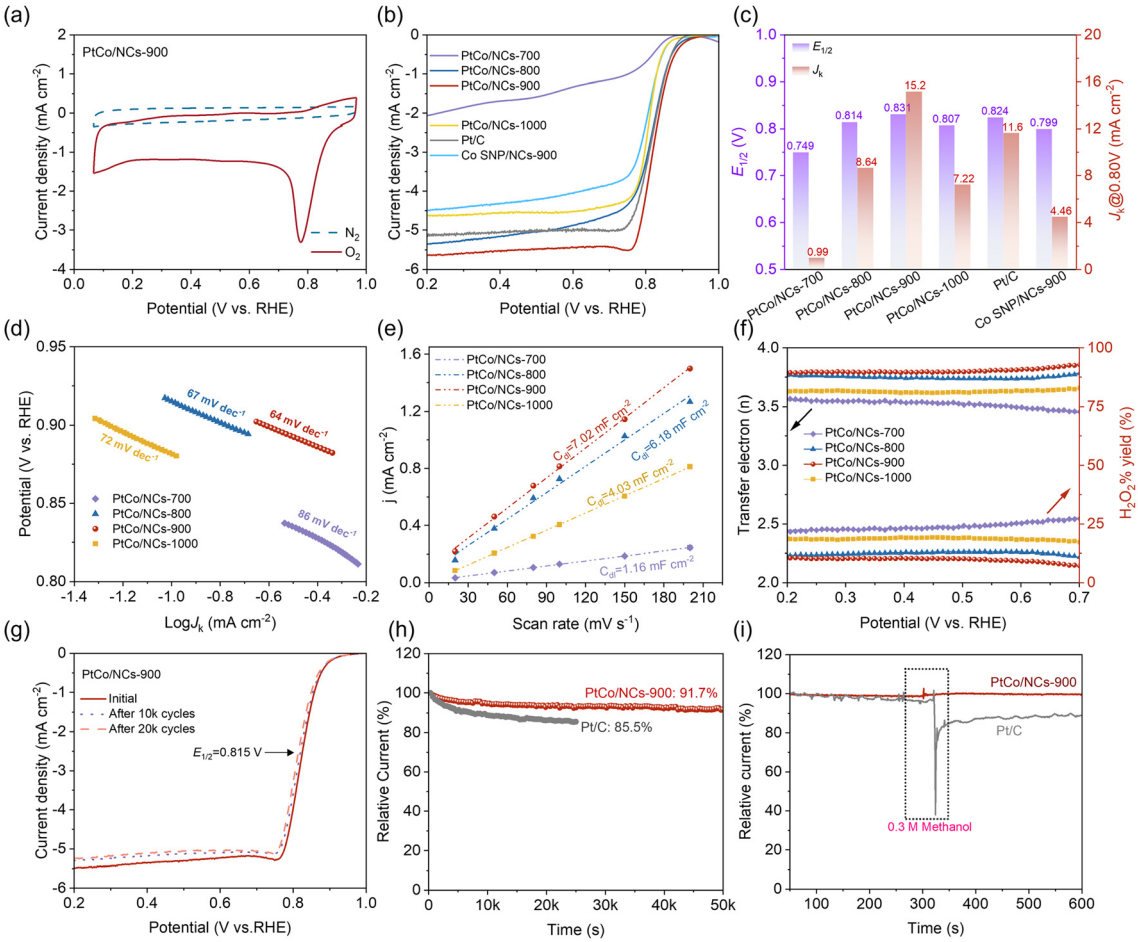

Fig. 6 (a) CV curves of PtCo/NCs-900 in N_2 and O_2-saturated 0.1 M KOH. (b) LSV curves at 1600 rpm in O_2-saturated 0.1 M KOH and (c) half-wave potential and kinetic current density data (j_k) of different samples and 20% Pt/C. (d) Tafel, (e) electrochemical double-layer capacitance (C_{dl}), and (f) electron transfer numbers (n) and peroxide yield (H_2O_2%) of different samples. (g) LSV curves of PtCo/NCs-900 before and after the accelerated durability test. (h) Chronoamperometric responses and (i) methanol tolerance test of PtCo/NCs-900 and 20% Pt/C with 10 mL of 0.3 M methanol at 0.7 V and 1600 rpm in O_2-saturated 0.1 M KOH.

Table 1 Comparison of the ORR performance of the prepared electrocatalysts and Pt/C

Samples	j_m (mA mg^{-1})	TOF (e^- per site per s)
PtCo/NCs-700	57.14	0.28
PtCo/NCs-800	502.08	2.45
PtCo/NCs-900	907.87	4.44
PtCo/NCs-1000	430.49	2.10
Pt/C	199.20	0.40

502.08 mA mg^{-1}, TOF = 2.45 e^- per site per s), PtCo/NCs-1000 (j_m = 430.39 mA mg^{-1}, TOF = 2.10 e^- per site per s) and 20% Pt/C (j_m = 199.20 mA mg^{-1}, TOF = 0.40 e^- per site per s).

Additionally, durability is a crucial factor for evaluating the commercial applicability of catalysts. Accelerated durability tests (ADTs) were performed on both PtCo/NCs-900 and Pt/C catalysts. As shown in Fig. 6g, the results showed that the $E_{1/2}$ of PtCo/NCs-900 decreased by only 16 mV after 20k CV cycles. In contrast, the $E_{1/2}$ of Pt/C exhibited a much larger negative shift of 25 mV after 10k CV cycles (Fig. S14). Chronoamperometric measurements were further employed to evaluate the durability of PtCo/NCs-900 (Fig. 6h). After 50 000 s, PtCo/NCs-900 retained 91.7% of its initial ORR current, demonstrating markedly superior durability compared with Pt/C, which retained only 85.5% of its initial current after 25 000 s. Fig. 6i illustrates the methanol tolerance tests of PtCo/NCs-900 and Pt/C. The relative current of PtCo/NCs-900 remains nearly unchanged upon methanol introduction. In contrast, Pt/C exhibits a pronounced decrease in the relative current, which cannot recover to its initial value. These results demonstrate that PtCo/NCs-900 possesses superior durability and methanol tolerance compared with Pt/C. The above results indicate that PtCo/NCs-900 exhibits excellent catalytic performance toward the ORR, which can be attributed to its moderately curved interface. Compared with previously reported PtCo-based electrocatalysts, PtCo/NCs-900 possesses a good ORR activity (Table S2). Specifically, the curved interface intensifies the local electric field and facilitates O_2 enrichment,

thereby accelerating electron transfer and ensuring a sufficient O_2 supply. Concurrently, the curved interface induces strong electronic interactions between Pt and Co atoms, which can optimize the binding strength of oxygen-containing intermediates and ultimately enhance the overall electrocatalytic activity.

To investigate the impact of the curved interface on the electronic structure of PtCo alloys, we conducted density functional theory (DFT) calculations.[51,52] Based on the synthesized samples, theoretical models of PtCo/NCs-700 and PtCo/NCs-900 were constructed (Fig. S15). The calculated charge-density distribution results (Fig. 7a) reveal that PtCo/NCs-900 exhibits significantly enhanced electron accumulation on the Pt atoms and the curved interfacial region, while the electron depletion at the Co atoms is more pronounced. This suggests that electrons are more readily transferred from the Co atoms to the Pt atoms and the curved carbon interface, thereby forming an electron-rich state. Furthermore, the projected density of states (PDOS) analysis for Pt (Fig. 7b) reveals that the d-band center of Pt atoms in PtCo/NCs-900 (−1.358 eV) is closer to the Fermi level than that of PtCo/NCs-700 (−1.403 eV) in the planar structure. This indicates that when the PtCo alloy is supported on a curved interface, the Pt atoms can have stronger charge transfer and electron donor capabilities towards O_2 molecules and reaction intermediates. Additionally, the d-band center of Co in PtCo/NCs-900 is located at −1.153 eV, which is lower than the −0.987 eV observed in PtCo/NCs-700 (Fig. S16). The electron density redistribution induced by the curved interface disrupts the original electronic structure, strengthening Pt–Co electronic coupling.

To verify why the PtCo alloy at the curved interface exhibits a superior intrinsic ORR activity compared with that at a planar interface, Gibbs free energy diagrams for the four-electron ORR pathway were constructed (Fig. 7c and d). At U = 0 V, all elementary reaction steps for both PtCo/NCs-700 and PtCo/NCs-900 show thermodynamically spontaneous trends (Fig. 7c). At the operating potential of U = 1.23 V (Fig. 7d), the rate-determining step (RDS) for both catalysts is identified as the desorption of *OH, indicating that the removal of terminal oxygenated intermediates is the key step limiting the reaction rate. Notably, the Gibbs free energy change of the RDS for PtCo/NCs-900 (ΔG = 0.86 eV) is significantly lower than that for PtCo/NCs-700 (ΔG = 0.99 eV), indicating that PtCo/NCs-900 requires less energy in the process of *OH desorption. This result can mainly be attributed to electron enrichment at the Pt sites of the PtCo alloy on the curved interface, which facilitates interactions between the surface electron and adsorbates, thereby weakening the *OH binding strength and promoting its desorption. Meanwhile, the electron accumulation at the curved interface enhances the interfacial electron transfer between PtCo and the carbon supports, achieving the supply and redistribution of electrons near the interface during the reaction. This enhanced electron transfer further reduces the energy barrier for the removal of *OH and thus accelerates the regeneration of active sites. Overall, the electron enrichment at the Pt sites and the curved interface synergistically optimize the *OH adsorption/desorption balance, endowing PtCo/NCs-900 a lower RDS free energy and superior ORR kinetics.

Based on the advantages in structure and catalytic performance, PtCo/NCs-900 was applied to a primary zinc–air battery (ZAB), in which a polished Zn plate with a thickness of 0.2 mm and the PtCo/NCs-900 catalyst-loaded carbon paper were used as the anode and the air cathode, respectively, and 6.0 M KOH/0.2 M $(CH_3COO)_2Zn$ was used as an electrolyte. The practical applicability of PtCo/NCs-900 was demonstrated by powering a light-emitting diode panel (inset of Fig. 8a). PtCo/NCs-900-based ZAB exhibits an open-circuit potential (OCP) of 1.43 V,

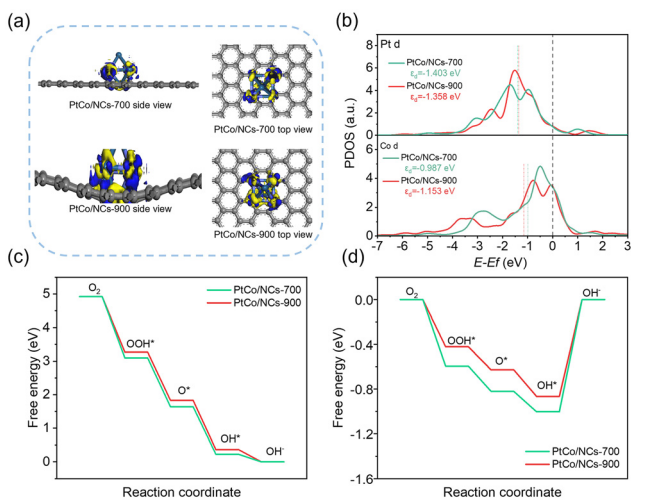

Fig. 7 (a) Differential charge densities of PtCo/NCs-700 and PtCo/NCs-900 (yellow: electron accumulation and blue: electron depletion). (b) PDOS of Pt 5d orbitals of PtCo/NCs-700 and PtCo/NCs-900. Gibbs free energy diagrams toward the ORR at equilibrium potentials (U) of (c) 0 and (d) 1.23 V.

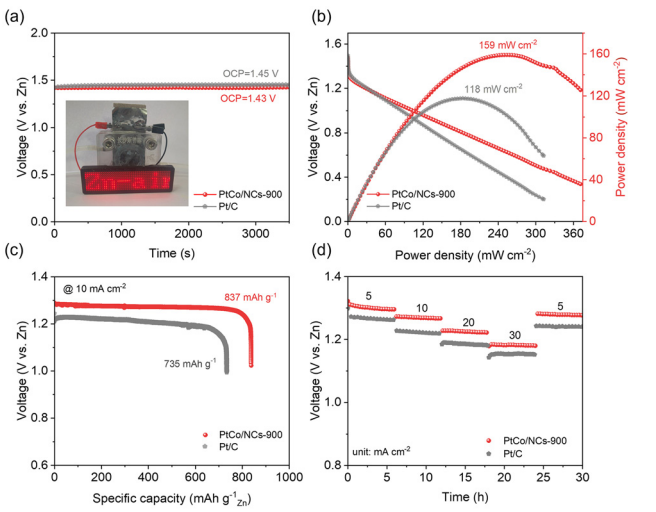

Fig. 8 Performance of assembled ZABs. (a) Open-circuit potential (OCP) curves (the inset shows a photograph of an LED display powered by the assembled ZABs). (b) Discharge curves and corresponding power density curves. (c) Specific capacities. (d) Galvanostatic discharge curves under different current densities.

which is comparable to that of Pt/C (1.45 V). The discharge polarization curves and corresponding power density curves (Fig. 8b) highlighted the superiority of ZAB with PtCo/NCs-900, delivering a peak power density of 159 mW cm^{-2} compared to 118 mW cm^{-2} for Pt/C. The gravimetric specific capacity calculated from zinc consumption reached 837 mAh g^{-1} for the ZAB with PtCo/NCs-900 (Fig. 8c), exceeding that of the ZAB with Pt/C (735 mAh g^{-1}). The discharge curves also demonstrate that the PtCo/NCs-900-based battery achieves higher discharge plateaus at various current densities along with better reversibility and rate performance (Fig. 8d). Additionally, the charge–discharge capability and long-term durability of the ZAB built with the PtCo/NCs-900 + RuO_2 catalyst couple were evaluated *via* galvanostatic charge–discharge cycling tests at a current density of 5 mA cm^{-2} (Fig. S17). The ZAB operated stably for over 100 h, demonstrating substantial potential for practical energy storage applications.

4. Conclusion

In summary, we proposed a rational design strategy for engineering curved interfaces within carbon supports to optimize the ORR electrocatalytic performance of the alloy catalysts. FEM simulations confirmed that a moderately curved interface intensifies the local electrostatic field and promotes O_2 enrichment. Guided by these predictive models, we successfully synthesized PtCo alloy nanoparticles anchored to N-doped carbon (PtCo/NCs), achieving high structural similarity with the simulated models. The PtCo/NCs-900 catalyst with a moderately curved interface exhibits an excellent ORR activity ($E_{1/2}$ = 0.831 V) and durability. DFT calculations reveal that the PtCo alloy located on the curved interface exhibits weaker binding strength toward key oxygenated intermediates during desorption. The presence of the curved interface not only lowers the energy barrier of the rate-determining step but also facilitates electron transfer and ensures an abundant supply of O_2, thereby synergistically enhancing electrocatalytic activity. The assembled Zn–air battery with the catalyst demonstrates a remarkable peak power density of 159 mW cm^{-2}, a high specific capacity of 837 mAh g^{-1}, and outstanding rate performance. This study reveals the correlation between curvature-engineered interfaces and catalytic activity, providing new insights for the rational design of high-efficiency ORR electrocatalysts.

Author contributions

Yutong Shi: writing – original draft, data curation. Zheyan Tang: writing – original draft, methodology. Hongwei Zhao: writing – review & editing, funding acquisition, data curation. Pengyi Sun: methodology. Lixiang Li: writing – review & editing, funding acquisition. Haifei Liu: methodology. Jingang Zheng: methodology. Lin Tao: software, methodology. Han Zhang: supervision. Fang Di: supervision. Chengguo Sun: supervision. Zhihao Yao: software. Yanzhou Qin: software. Baigang An: writing – review & editing, supervision, resources, methodology, funding acquisition, data curation.

Conflicts of interest

The authors declare that they have no known competing financial interests or personal relationships that could have appeared to influence the work reported in this paper.

Data availability

The authors confirm that the data supporting the findings of this study are available within the article and its supplementary information (SI). Supplementary information is available. See DOI: https://doi.org/10.1039/d6nr01476c.

Acknowledgements

We acknowledge the financial support by the grants from the National Natural Science Foundation of China (51872131, 52371224, and 51972156), the Startup Fund for Doctoral Research of Liaoning (2023-BS-184), the University of Science and Technology Liaoning Talent Project Grants (6003000315), and the Fundamental Research Funds for the Liaoning Universities (LJ222410146062 and LJ212410146075).

References

1 Z. W. Seh, J. Kibsgaard, C. F. Dickens, I. Chorkendorff, J. K. Nørskov and T. F. Jaramillo, *Science*, 2017, **355**, eaad4998.
2 S. Wang and S. P. Jiang, *Natl. Sci. Rev.*, 2017, **4**, 163–166.
3 H. W. Zhao, T. Y. Xing, L. X. Li, X. Geng, K. Guo, C. G. Sun, W. M. Zhou, H. M. Yang, R. F. Song and B. G. An, *Int. J. Hydrogen Energy*, 2019, **44**, 25180–25187.
4 K. M. Tan, T. S. Babu, V. K. Ramachandaramurthy, P. Kasinathan, S. G. Solanki and S. K. Raveendran, *J. Energy Storage*, 2021, **39**, 102591.
5 X. W. Lv, Z. Wang, Z. Lai, Y. Liu, T. Ma, J. Geng and Z. Y. Yuan, *Small*, 2024, **20**, 2306396.
6 L. Wu, L. X. Li, H. Zhang, H. W. Zhao, Q. D. Li, X. Y. Zhang, C. G. Sun and B. G. An, *Chem. Rec.*, 2026, e70182.
7 J. M. V. Nsanzimana, L. Cai, Z. Jiang, B. Y. Xia and T. Maiyalagan, *Nano-Micro Lett.*, 2025, **17**, 294.
8 Z. Y. Tang, H. W. Zhao, L. Tao, W. H. Liu, L. X. Li, Y. T. Shi, J. G. Zheng, L. Wu, H. Zhang, F. Di, C. G. Sun, Z. H. Yao, Y. Z. Qin and B. G. An, *Int. J. Hydrogen Energy*, 2026, **228**, 154698.
9 A. Zadick, L. Dubau, N. Sergent, G. Berthomé and M. Chatenet, *ACS Catal.*, 2015, **5**, 4819–4824.
10 H. W. Zhao, Y. Q. Chen, H. Y. Zuo, L. Li, L. X. Li, F. F. Ai, Z. Y. Tang, T. Y. Xing, Y. Q. Zhang, L. Tao, Z. W. Tian,

H. M. Yang, X. Geng and B. G. An, *Catal. Today*, 2024, **438**, 114811.
11 L. Chong, J. Wen, J. Kubal, F. G. Sen, J. Zou, J. Greeley, M. Chan, H. Barkholtz, W. Ding and D. J. Liu, *Science*, 2018, **362**, 1276–1281.
12 J. H. Kim, S. Y. Lee, H. J. Lee, H. I. Lee, D. H. Lim, Y. S. Lee, H. S. Kim and S. H. Woo, *ACS Eng. Au*, 2025, **5**, 1–9.
13 V. R. Stamenkovic, B. S. Mun, M. Arenz, K. J. J. Mayrhofer, C. A. Lucas, G. Wang, P. N. Ross and N. M. Markovic, *Nat. Mater.*, 2007, **6**, 241–247.
14 M. Zhou, S. Bao and A. J. Bard, *J. Am. Chem. Soc.*, 2019, **141**, 7327–7332.
15 S. Lee, Y. Kang, J. Lee, J. Kim, J. W. Shin, S. Sim, D. Go, E. Jo, S. Kye, J. Kim and J. An, *Appl. Surf. Sci.*, 2022, **571**, 151256.
16 D. Li, X. Chen, Y. Lv, G. Zhang, Y. Huang, W. Liu, Y. Li, R. Chen, C. Nuckolls and H. Ni, *Appl. Catal., B*, 2020, **269**, 118824.
17 P. Gao, M. Pu, Q. Chen and H. Zhu, *Catalysts*, 2021, **11**, 1050.
18 S. Liu, H. Xu, D. Liu, H. Yu, F. Zhang, P. Zhang, R. Zhang and W. Liu, *J. Am. Chem. Soc.*, 2021, **143**, 15243–15249.
19 L. Huang, S. Zaman, X. Tian, Z. Wang, W. Fang and B. Y. Xia, *Acc. Chem. Res.*, 2021, **54**, 311–322.
20 F. D. Speck, M. T. Y. Paul, F. Ruiz-Zepeda, M. Gatalo, H. Kim, H. C. Kwon, K. J. J. Mayrhofer, M. Choi, C. H. Choi, N. Hodnik and S. Cherevko, *J. Am. Chem. Soc.*, 2020, **142**, 15496–15504.
21 H. Wang, J. X. Liu, L. F. Allard, S. Lee, J. Liu, H. Li, J. Wang, J. Wang, S. H. Oh, W. Li, M. Flytzani-Stephanopoulos, M. Shen, B. R. Goldsmith and M. Yang, *Nat. Commun.*, 2019, **10**, 3808.
22 Y. Qin, X. Han, S. Gadipelli, J. Guo, S. Wu, L. Kang, J. Callison and Z. Guo, *J. Mater. Chem. A*, 2019, **7**, 6543–6551.
23 M. Zhang, T. Zhou, D. Bukhvalov, F. Han, C. Wang and X. Yang, *Appl. Catal., B*, 2023, **337**, 122976.
24 G. Luo, M. Song, L. An, X. Huang, Q. Zhang, C. Zhang, T. Shen, S. Wang and D. Wang, *J. Energy Chem.*, 2025, **100**, 721–729.
25 Z. Chen, H. Qing, K. Zhou, D. Sun and R. Wu, *Prog. Mater. Sci.*, 2020, **108**, 100618.
26 F. Guo, Z. Zou, Z. Zhang, T. Zeng, Y. Tan, R. Chen, W. Wu, N. Cheng and X. Sun, *J. Mater. Chem. A*, 2021, **9**, 5468–5474.
27 R. Mo, X. Zhang, Z. Chen, S. Huang, Y. Li, L. Liang, Z. Q. Tian and P. K. Shen, *Int. J. Hydrogen Energy*, 2021, **46**, 15991–16002.
28 B. B. Xu, X. B. Fu, X. M. You, E. Zhao, F. F. Li, Z. Chen, Y. X. Li, X. L. Wang and Y. F. Yao, *ACS Catal.*, 2022, **12**, 6958–6967.
29 W. Chen, X. Zhu, W. Wei, H. Chen, T. Dong, R. Wang, M. Liu, K. Ostrikov, P. Peng and S. Q. Zang, *Small*, 2023, **19**, 2304294.
30 L. Zheng, S. Gao, S. Yao, Y. Huang, S. Zhai, J. Hao, X. Fu, Q. An and Z. Xiao, *J. Colloid Interface Sci.*, 2024, **674**, 735–744.
31 H. Chen, X. Liang, Y. Liu, X. Ai, T. Asefa and X. Zou, *Adv. Mater.*, 2020, **32**, 2002435.
32 Z. Liang, T. Qiu, S. Gao, R. Zhong and R. Zou, *Adv. Energy Mater.*, 2022, **12**, 2003410.
33 N. Ramaswamy, W. Gu, J. M. Ziegelbauer and S. Kumaraguru, *J. Electrochem. Soc.*, 2020, **167**, 064515.
34 Y. Zhang, J. Lan, Y. Xu, Y. Yan, W. Liu, X. Liu, S. Gu, J. Zhou and M. Wang, *J. Colloid Interface Sci.*, 2024, **660**, 997–1009.
35 D. Huang, X. Zhan, L. Tian, L. Cao, L. Lei, J. Xiong, L. Zhou, J. Tian and X. Tong, *J. Alloys Compd.*, 2025, **1039**, 182983.
36 X. Zhao, Y. Wang, J. Wen, L. Cao, F. Wang, K. Lei, R. Fang, L. Zhou and Y. Li, *J. Am. Chem. Soc.*, 2025, **147**, 19166–19177.
37 Y. Zhu, Y. Jiang, H. Li, D. Zhang, L. Tao, X. Z. Fu, M. Liu and S. Wang, *Angew. Chem., Int. Ed.*, 2024, **63**, e202319370.
38 H. Wang, H. Xu, F. Yang, Y. Qing, F. Chu, Y. Wu, S. Ye and F. Xiong, *Adv. Mater.*, 2026, **38**, e15230.
39 Y. Xie, X. Dong, W. Hu, D. Wang, Y. Peng, R. Zou, X. Xiao, H. Cui, C. Zhang, C. C. Hou and Q. Xu, *Chem Catal.*, 2025, **5**, 101367.
40 J. Gahtori, C. L. Tucker, T. S. Khan, C. de Sá Codeço, T. Rocha and A. Bordoloi, *ACS Appl. Mater. Interfaces*, 2022, **14**, 38905–38920.
41 X. Yu, Y. Xie, X. Dong, D. Wang, T. Sun, Q. Sun, S. Cao, F. Meng, R. Zou, C. Zhang, Q. Xu and C. C. Hou, *Adv. Funct. Mater.*, 2025, **35**, 2424401.
42 W. Yang, L. Zou, Q. Huang, Z. Zou, Y. Hu and H. Yang, *J. Electrochem. Soc.*, 2017, **164**, H331.
43 Y. Hu, X. Guo, T. Shen, Y. Zhu and D. Wang, *ACS Catal.*, 2022, **12**, 5380–5387.
44 H. D. Mai, P. M. Park, G. N. Bae, S. Jeong, B. Seo, M. Cho, S. Park, N. D. Cuong, T. V. Cuong, N. M. Tran, C. M. Park and K. J. Jeon, *J. Mater. Chem. A*, 2024, **12**, 4761–4769.
45 H. W. Zhao, L. X. Li, H. Y. Zuo, D. Qu, H. Zhang, L. Tao, C. G. Sun, D. Y. Ju and B. G. An, *New Carbon Mater.*, 2023, **38**, 861–874.
46 Z. Y. Tang, H. W. Zhao, M. Y. Chen, L. X. Li, S. Q. Guan, L. Wu, H. Y. Zuo, H. Zhang, J. G. Zheng, L. Tao, C. G. Sun, Q. D. Li, X. Y. Zhang and B. G. An, *J. Alloys Compd.*, 2026, **1068**, 188545.
47 N. Ji, H. Sheng, S. Liu, Y. Zhang, H. Sun, L. Wei, Z. Tian, P. Jiang, Q. Chen and J. Su, *Nano Res.*, 2024, **17**, 7900–7908.
48 H. W. Zhao, Y. Q. Zhang, L. X. Li, X. Geng, H. M. Yang, W. M. Zhou, C. G. Sun and B. G. An, *Chin. Chem. Lett.*, 2021, **23**, 140–145.
49 K. Song, F. Kong, R. Shen, X. Yu, H. Tian, Q. Guo, G. Zhang, W. Sun and X. Cui, *J. Mater. Chem. A*, 2025, **13**, 6407–6416.
50 Y. J. Zhao, L. Y. Zhu, J. Tang, L. Fu, D. Jiang, X. Q. Wei, H. Nara, T. Asahi and Y. Yamauchi, *ACS Nano*, 2024, **18**(1), 373–382.
51 C. Yan, W. An, T. Shen, L. Ma, M. Zhang, F. Gao, T. Yang, C. Wang, G. Huang and S. Xu, *J. Mater. Chem. A*, 2023, **11**, 26812–26820.
52 Q. Wang, L. Lyu, X. Hu, W. Fan, C. Shang, Q. Huang, Z. Li, Z. Zhou and Y. M. Kang, *Angew. Chem., Int. Ed.*, 2025, **64**, e202422920.